# Experimental exploration of a mixed helium/carbon beam for online treatment monitoring in carbon ion beam therapy

# Experimental exploration of a mixed helium/carbon beam for online treatment monitoring in carbon ion beam therapy

**L. Volz**[1,2,†]**, L. Kelleter**[3,†]**, S. Brons**[5]**, L. Burigo**[6,7]**, C. Graeff**[4]**, N. I. Niebuhr**[6,7,2]**, R. Radogna**[3]**, S. Scheloske**[5]**, C. Schömers**[5]**, S. Jolly**[3] **and J. Seco**[1,2]

[1] Department of Biomedical Physics in Radiation Oncology, German Cancer Research Centre (DKFZ), Heidelberg, GER

[2] Department of Physics and Astronomy, Heidelberg University, Heidelberg, GER

[3] Department of Physics and Astronomy, University College London, London, UK

[4] Biophysics division, GSI Helmholtzzentrum für Schwerionenforschung GmbH, Darmstadt, GER

[5] Heidelberg Ion-Beam Therapy Centre (HIT), Heidelberg, GER

[6] Department of medical physics in radiation oncology, German Cancer Research Centre (DKFZ), Heidelberg, GER

[7] Heidelberg Institute for Radiation Oncology (HIRO), National Centre for Radiation Research in Oncology (NCRO), Heidelberg, GER

[†] Authors contributed equally

E-mail: `l.volz@dkfz-heidelberg.de`, `laurent.kelleter@ucl.ac.uk`

**Abstract.**

Recently, it has been proposed that a mixed helium/carbon beam could be used for online monitoring in carbon ion beam therapy. Fully stripped, the two ion species exhibit approximately the same mass/charge ratio and hence could potentially be accelerated simultaneously in a synchrotron to the same energy per nucleon. At the same energy per nucleon, helium ions have about three times the range of carbon ions, which could allow for simultaneous use of the carbon ion beam for treatment and the helium ion beam for imaging. In this work, measurements and simulations of PMMA phantoms as well as anthropomorphic phantoms irradiated sequentially with a helium ion and a carbon ion beam at equal energy per nucleon are presented. The range of the primary helium ion beam and the fragment tail of the carbon ion beam exiting the phantoms were detected using a novel range telescope made of thin plastic scintillator sheets read out by a flat-panel CMOS sensor. A 10:1 carbon to helium mixing ratio is used, generating a helium signal well above the carbon

*Mixed helium/carbon beam* 2

fragment background while adding little to the dose delivered to the patient. The range modulation of a narrow air gap of 1 mm thickness in the PMMA phantom that affects less than a quarter of the particles in a pencil beam were detected, demonstrating the achievable relative sensitivity of the presented method. Using two anthropomorphic pelvis phantoms it is shown that small rotations of the phantom as well as simulated bowel gas movements cause detectable changes in the helium/carbon beam exiting the phantom. The future prospects and limitations of the helium-carbon mixing as well as its technical feasibility are discussed.

## 1. Introduction

The advantage of carbon-beam therapy over conventional photon radiotherapy lies in the ion's highly localised depth-dose deposition, with a low entrance dose increasing to a maximum — the Bragg peak — beyond which there is a sharp reduction in dose deposition. However, the steep dose gradient at the end of the particle range in matter makes ion beam therapy sensitive to range uncertainties arising, for example, from inter- and intra-fractional anatomical changes, uncertainties at the treatment planning stage as well as the patient setup. In current clinical practice, range uncertainties are accounted for by adding safety margins around the tumour volume (Paganetti 2012) and by avoiding beam directions corresponding to the ions stopping directly in front of an organ at risk (OAR). However, even with safety margins, intra-fractional motion can lead to severe target dose deterioration and/or over-dosage of healthy tissue (Bert et al. 2008, Seco et al. 2009, Dolde et al. 2018).

In order to exploit the full potential of ion beam radiotherapy, therefore, improved methods for inter- and intra-fractional treatment verification are needed. Several methods for treatment verification have been proposed of which prompt gamma imaging (Hueso-González et al. 2018) and in-beam PET imaging (Ferrero et al. 2018) are promising candidates. A detailed overview can be found in Parodi & Polf (2018).

Recently, it has been proposed that a small percentage of helium ions could be added to a carbon ion treatment beam for online treatment monitoring (Graeff

*Mixed helium/carbon beam* 3

23  et al. 2018, Mazzucconi et al. 2018). The approximately equal mass/charge ratio
24  of fully stripped helium and carbon ions (relative difference $\approx 0.065\,\%$), could
25  enable their simultaneous acceleration in a synchrotron accelerator to the same
26  velocity (same energy per nucleon). Due to the helium ions' $\sim 3$ times larger
27  range compared to that of carbon ions at the same velocity, treatment with a
28  carbon ion beam and simultaneous treatment monitoring with helium ions could
29  be possible. In fact, the similarity in accelerator settings for the delivery of a
30  mixed helium/carbon beam ($^{12}C^{4+}$ with $^{3}He^{+}$) has been reported already in Kanai
31  et al. (1997) for a cyclotron facility for the purpose of treatment with beams of
32  mixed relative biological effectiveness (RBE) but without consideration for online
33  treatment monitoring. Recently, Graeff et al. (2018) have shown the potential of
34  using a mixed helium/carbon beam as a range probe for carbon ion treatment
35  investigating lung patient cases using based on 4D treatment planning. Assuming
36  a fixed helium contamination in the primary carbon ion beam during the plan
37  optimisation, they showed that the additional RBE dose stemming from a $10\,\%$
38  helium contamination in the primary beam would make up less than $0.5\,\%$ of
39  the target RBE dose. This stems from the physical dose difference between the
40  plateau region of the helium ion depth dose profile and the carbon Bragg peak,
41  as well as the difference in RBE. Moreover, the dose deposited in the patient
42  distal to the tumor stemming from the additional helium contamination was also
43  smaller compared to that deposited by the carbon fragments. The idea of a mixed
44  beam for treatment monitoring was first explored experimentally in the study
45  presented recently by Mazzucconi et al. (2018). In their proof-of-concept work,
46  they demonstrated that for a $10\,\%$ mix of helium ions in the carbon beam, the
47  helium residual range could be detected in a scintillation detector despite the signal
48  contamination with carbon fragments. However, all experimental tests presented
49  were conducted using protons in place of helium ions and no anthropomorphic
50  cases were investigated.

51      The aim of this work was therefore to experimentally corroborate the results
52  by Graeff et al. (2018) and Mazzucconi et al. (2018) using sequentially irradiated
53  beams of helium and carbon ions at the Heidelberg Ion-Beam Therapy Centre
54  (HIT). The beam was monitored using a novel range telescope developed at
55  University College London (UCL). First, the system's sensitivity was assessed
56  with simple PMMA degraders with differently sized air gaps. For assessing
57  more clinically relevant scenarios, prostate cancer treatments were investigated.
58  With the ADAM pelvis phantom (Niebuhr et al. 2019), the feasibility of using
59  a mixed helium/carbon beam to detect rectal gassing/bowel gas movements was

*Mixed helium/carbon beam* 4

investigated. The recently developed ADAM-PETer pelvis phantom (Homolka et al. 2019) was used to simulate small patient rotations. The acquired data allow to draw conclusions on the clinical application and the limitations of the helium/carbon beam mixing method.

## 2. Materials and Methods

### 2.1. Range telescope

The range of the primary helium ions and the fragments produced by the carbon ion beam were monitored using a novel range telescope developed at UCL for proton range quality assurance. This detector will be detailed in a separate publication currently under preparation. The prototype detector consisted of a stack of 49 polystyrene-based plastic scintillator sheets of 2-3 mm thickness, covered an area of $10 \times 10 \, \text{cm}^2$, and had a relative stopping power (RSP) of 1.025. The detector covered a total water equivalent thickness (WET) range of $\sim 127 \, \text{mm}$. Each sheet was painted black in order to avoid light contamination into neighbouring sheets. The resulting thickness of paint was taken into account in the calculation of the absolute WET.

A large-area CMOS sensor with an active area of $150 \times 100 \, \text{mm}^2$ and a pixel size of $100 \, \mu\text{m}$ was used for the readout of the scintillation light. The detector readout frame rate was $25 \, \text{Hz}$ ($40 \, \text{ms}$ exposure time). The detector was placed in a light-tight enclosure with two beam entrance/exit windows made of aluminum coated Mylar polyester foil on both ends of the scintillator stack.

Before the measurements, the detector was calibrated by shooting high-energy beams of carbon ions ($\text{E}=430 \, \text{MeV/u}$) as well as helium ions ($\text{E}=220 \, \text{MeV/u}$) through the scintillator stack from both sides of the detector. In data processing, these shoot-through measurements were then used to correct for non-uniformity in the light output of each individual detector sheet for each ion species. Additionally, a background measurement was acquired to determine the signal in the absence of scintillation light.

It is important to note that the range telescope measures scintillation light and not dose. The plastic scintillator used in the range telescope exhibits quenching effects that can be described by Birks' law (Birks 1951). The measured depth-light curves presented in this work were not corrected for quenching: however, the simulated energy deposits were converted to depth-light curves using Birks' law (see section 2.4). Additionally, the measured light output of the detector depends

94 on the lateral position at which the beam enters the detector. In this work, the
95 detector position relative to the beam was not changed between measurements.

96 *2.2. Investigated phantoms*

97 Three different phantom setups were investigated in this study. The sensitivity
98 and limitation of the method was assessed quantitatively using simple PMMA
99 phantoms. For qualitatively investigating the use of a mixed helium/carbon
100 beam in clinically relevant scenarios, different motion scenarios were explored
101 using two anthropomorphic phantoms. Treatment planning X-ray CT scans of
102 the anthropomorphic phantoms were acquired at the Siemens Somatom Definition
103 Flash scanner of the German Cancer Research Centre (DKFZ, Heidelberg).

104 *PMMA phantom:*    First, several PMMA slabs were arranged upstream of the
105 range telescope to quantify the sensitivity of the method in a controlled setting.
106 Accurate WET values for each of the slabs were available from PTW Peakfinder
107 measurements (Arico 2016). In order to create a range shift in the beam, two thin
108 PMMA slabs of similar WET were placed at a depth of 49.6 mm PMMA (57.64 mm
109 WET) such that they formed a vertical slit of adjustable opening width (2-5 mm).
110 Different PMMA slabs were used to create variable gap thicknesses (1-5 mm). The
111 total WET of the setup (without gap) was 219.59 mm for all measurements. The
112 schematic setup is shown in figure 1.

113 *ADAM phantom:*    The ADAM (Anthropomorphic Deformable And Multi-
114 modal) Pelvis Phantom (Niebuhr et al. 2019) was used to demonstrate the effect of
115 rectal gassing/bowel gas movements on the helium range. The phantom consists
116 of various tissue equivalent materials enclosed in an elliptical PMMA container
117 (370 mm major, 220 mm minor axis) and closely models the anatomical structure
118 of a male pelvis. The phantom features a fully deformable and movable prostate, an
119 inflatable rectum and a deformable bladder, as well as the pelvic bone structures.
120 To simulate rectal gassing/bowel gas movements, a rectal balloon was inserted into
121 the phantom's rectum such that the balloon was located next to the prostate. The
122 balloon was inflated to air volumes of 30 ml, 45 ml and 60 ml. The uncertainty
123 on the air volume was estimated to be $\sim$5 ml from the retained air volume after
124 irradiation. Liquid fillings were not yet possible with the phantom and the rectum
125 was not collapsed when the rectal balloon was not inflated, but retained a residual
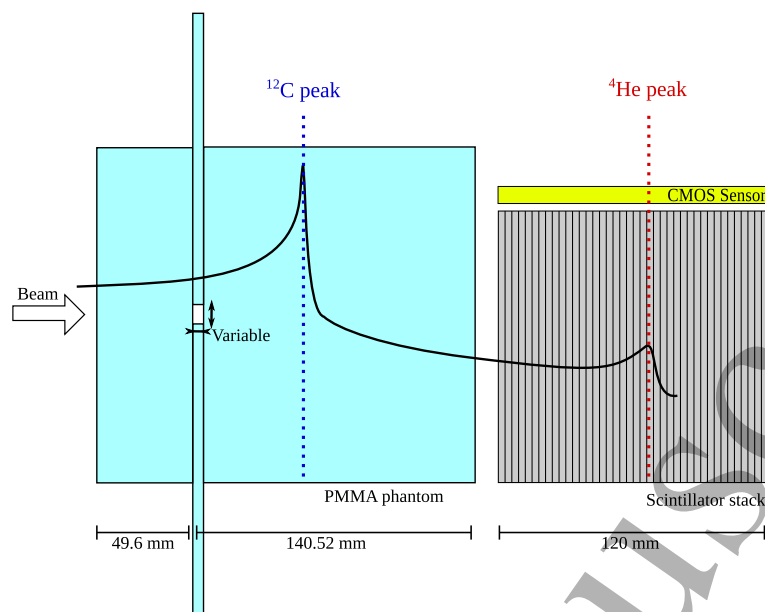126 volume.

*Mixed helium/carbon beam*                                                        6



**Figure 1.** Schematic depiction of the PMMA setup used to investigate the sensitivity of the helium/carbon beam mixing method (not to scale). The total thickness of the PMMA setup was $190.12\,\mathrm{mm}$ ($219.59\,\mathrm{mm}$ WET), the PMMA blocks had a width and height of $150\,\mathrm{mm}$. Two PMMA slabs of equal thickness were used to create a vertical slit of variable width/thickness at a depth of $49.6\,\mathrm{mm}$ in the setup. For the investigated energy in this work, the carbon peak was located at a water equivalent depth of $\sim 99\,\mathrm{mm}$, with the helium peak was located at $305\,\mathrm{mm}$ water equivalent depth.

*ADAM-PETer phantom:* In order to investigate the effect of patient rotations, the recently developed second generation of the ADAM phantom, named ADAM-PETer (Homolka et al. 2019), was used. Compared to the ADAM phantom, the ADAM-PETer phantom has a smaller container ($310\,\mathrm{mm}$ major, $195\,\mathrm{mm}$ minor axis), denser and more realistic bone structures as well as a 3D printed prostate. The reason for using both available ADAM phantoms in this study resides in their respective advantages/disadvantages. The ADAM phantom hull was made from two separate PMMA pieces that are glued together on both lateral sides (see figure 2). Additionally, the thickness gradient of the ADAM phantom hull is larger compared to that of the newer ADAM-PETer phantom. Hence, for investigation of patient rotations/motion, observed effects could stem from the glue or the phantom shape, rather than anatomical features which would not resemble a realistic scenario. However, the available version of the ADAM-PETer phantom did not feature a fully deformable/movable prostate and rectum, which
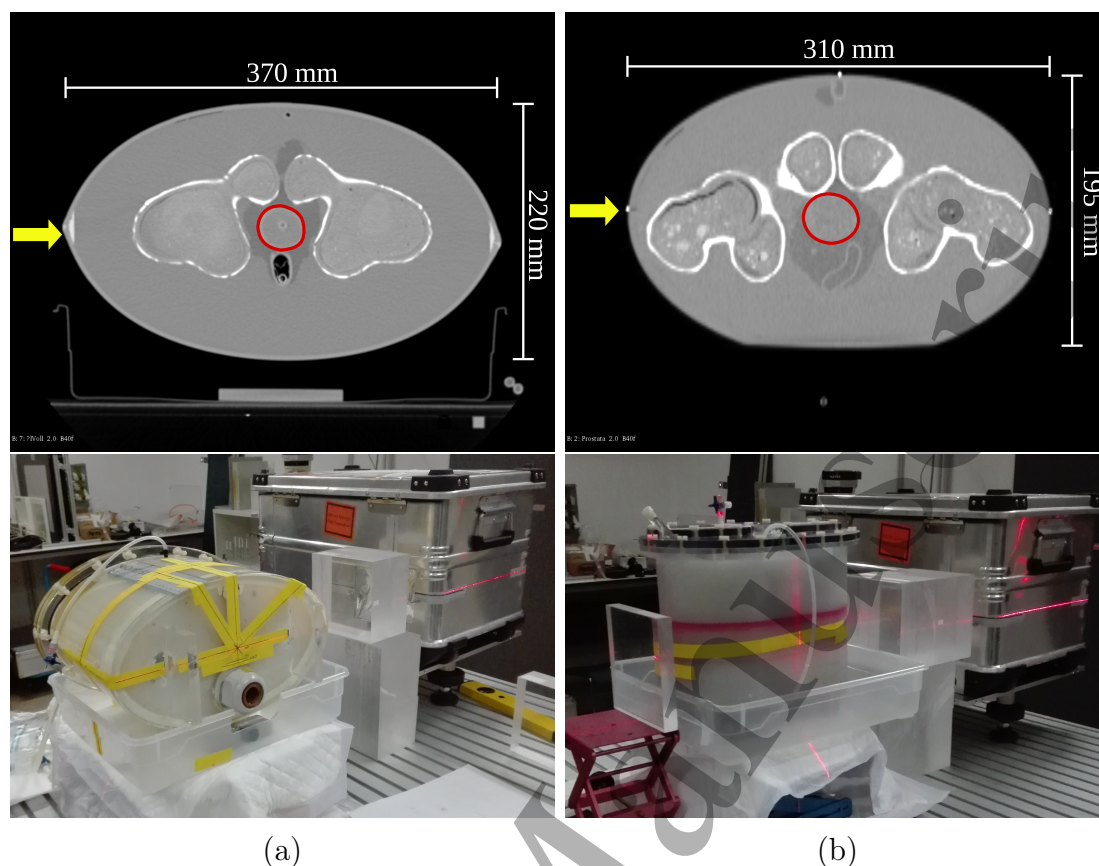
**Figure 2.** Isocentrical axial slice through CT images of the used phantoms (top), and photographs of the experimental setup (bottom): a) ADAM phantom and b) ADAM-PETer phantom. The area outlined in red on the CT scans marks the target (prostate), the yellow arrow indicates the beam direction.

141 would have been unfavourable for the investigation of rectal gassing.

142 *Treatment planning:* For the anthropomorphic pelvis phantoms, treatment
143 plans were generated using the MatRad open source treatment planning platform
144 (Wieser et al. 2017). A dose of 2 Gy RBE per fraction was planned for the target
145 (whole prostate). The spot spacing was set to 3 mm. No OARs were considered
146 and no margins were set around the target volume. The additional dose from the
147 helium beam was not considered in the treatment optimization. The minimum
148 and maximum beam energy in the plan as well as planned beam angles are listed
149 in table 1. The prostate was positioned in the beam isocentre in all cases.

*Mixed helium/carbon beam*                                                                 8

**Table 1.** Treatment plan minimum and maximum energies for the different phantoms. The 0° gantry angle refers to a vertical beam direction.

| Phantom | Gantry Angle (°) | Min. E (MeV/u) | Max. E (MeV/u) |
|---------|------------------|----------------|----------------|
| ADAM | [90, -90] | 300 | 355 |
| ADAM-PETer | [90, -90] | 260 | 316 |

**Table 2.** Beam settings for the different experimental setups investigated in this work. The beam focus is given as the beam FWHM at the isocentre.

| Setup | Energy (MeV/u) | | Focus (mm) | | Intensity (part./s) | |
|-------|---------|---------|---------|---------|---------|---------|
| | $^{12}C$ | $^{4}He$ | $^{12}C$ | $^{4}He$ | $^{12}C$ | $^{4}He$ |
| PMMA phantom | 219.8 | 220.5 | 8.5 | 8.1 | $8\times10^{7}$ | $8\times10^{7}$ |
| ADAM/ADAM-PETer | 324.26 | 324.26 | 8.0 | 7.0 | $8\times10^{7}$ | $7\times10^{8}$ |

### 2.3. Beam settings

151 Experiments were conducted at the HIT experimental room (Haberer et al. 2004).
152 Since a real mixed beam could not yet be delivered, the experiments were
153 conducted with sequentially irradiated helium and carbon ion beams of similar
154 energy/nucleon and similar spot size. The measurements from the sequentially
155 irradiated beams were mixed offline which will be detailed in section 2.5. The
156 generation of a mixed beam will be discussed in section 4.3. For all measurements,
157 a 3 mm ripple filter was used following the common practice with carbon ion
158 treatments at HIT. The detailed beam settings for the respective phantom setups
159 are listed in table 2. The generation of a real mixed beam is further discussed in
160 section 4.

161 Energies up to $\sim$220 MeV/u were available for both carbon and helium ions
162 from the standard libraries of beam characteristics used at HIT (Kleffner et al.
163 2009). As no perfect match between helium and carbon ion beam settings existed
164 in these tables, the closest representation was chosen for the PMMA measurements.
165 The highest clinically available beam intensity of $8\times10^{7}$ particles/second for carbon
166 ions would — assuming a constant ratio of 10:1 between primary carbon and helium
167 ions — correspond to an intensity of $8\times10^{6}$ particles/second for helium ions in the
168 mixed beam. This is lower than the lowest helium intensity available from the
169 standard settings. Since the runs were mixed off-line in data processing, the same
170 intensity was therefore chosen for both ion types. The impact of this is discussed

*Mixed helium/carbon beam* 9

171 in section 4.

172 Due to the high carbon beam energy required for the treatment of the prostate
173 targets within the pelvis phantoms, a helium beam with manual settings had to
174 be used, since the corresponding high helium energies are not available from the
175 standard beam libraries at HIT which cover a maximum range in water of 30 cm for
176 the different ion species. However, since the HIT synchrotron was designed for the
177 acceleration of carbon ions up to 430 MeV/u, the synchrotron has the potential to
178 accelerate helium ions (and protons) to higher energies than those used clinically.
179 Helium ion beams, with higher energies than needed for therapy, have recently been
180 established at HIT in a preliminary version, for a few energies only and without
181 scanning capability or position and intensity control. In this work, a helium beam
182 at 326 MeV/u was used, with an intensity of $7 \times 10^8$ particles/second and a beam
183 focus of 7 mm FWHM.

184 For the ADAM-PETer phantom, a 20 mm PMMA slab was added before the
185 setup, as the available high helium energy would have been above the energies set
186 by the treatment plan. With the PMMA slab, the beam energy was reduced to
187 $\sim 303$ MeV/u for carbon ions (value obtained from the simulation described below),
188 corresponding to the high energy part of the respective treatment plan.

189 *2.4. Monte Carlo simulation*

190 In order to validate the acquired measurements and to further exploit the
191 potential of the helium/carbon beam mixing technique, Monte Carlo simulations
192 using Geant4 version 10.05.0 (Agostinelli et al. 2003, Allison et al. 2006,
193 Allison et al. 2016) were conducted. In detail, the following physics
194 lists were activated: G4DecayPhysics, G4StoppingPhysics for nuclear capture
195 at rest, G4EmExtraPhysics and G4EmStandardPhysics_option4 for accurate
196 modelling of low energy electromagnetic interactions, G4HadronElasticPhysics for
197 modelling of elastic nuclear interactions. To model inelastic nuclear interactions
198 the G4QMDReaction model was chosen for carbon ions as recommended
199 by Böhlen et al. (2010) and Dudouet et al. (2014). For helium ions,
200 G4BinaryLightIonReaction was activated together with the Tripathi cross section
201 data (Tripathi et al. 1999) recently tuned by Horst et al. (2019) to accurately
202 model the helium Bragg peak. The default production cuts (affecting electrons
203 and photons) were set in the simulation to 1 mm. Within the range telescope a
204 finer step limit and finer production cuts (both 0.05 mm) were set.

205 The helium and carbon energy spectra after the 3 mm ripple filter were

*Mixed helium/carbon beam* 10

206 modelled from the generic beam line presented in Wieser et al. (2017). The beam
207 monitoring chambers were modelled in the generic beam line using a water slab
208 of 2.03 mm thickness. The distance between nozzle and isocentre was 1.02 m (air,
209 RSP=0.001). Therefore, the WET the beam crossed before reaching the isocentre
210 was 3.05 mm. The lateral beam profile was modelled with a 2D Gaussian spatial
211 distribution with the FWHM set in the experiments. The initial beam divergence
212 was neglected in the simulation.

213     The detector was modelled as a single $100 \times 100 \times 120 \, \text{mm}^3$ block of polystyrene
214 using the polystyrene material composition from the NIST database (Berger
215 et al. 2005) and modifying the density to match the known RSP of 1.025. Within
216 the simulation, the energy deposit in the detector was binned along the condensed-
217 history steps into a histogram for which the bins corresponded to the sheets of
218 the prototype†. In order to accurately model the light output of the experimental
219 measurement, the scintillation light quenching has been approximated using Birks'
220 law (Birks 1951). The scintillation light output $S$ is given as:

$$221 \qquad S \propto \int \frac{\mathrm{d}E/\mathrm{d}x}{1 + kB\mathrm{d}E/\mathrm{d}x} \mathrm{d}x \qquad (1)$$

222     where Birks' constant was determined as $kB = 0.075 \pm 0.01 \, \text{mm/MeV}$ by
223 comparing proton beam measurements with the detector and HIT base data proton
224 depth dose curves (unpublished data). To accurately model the detector response
225 across the transverse plane, $S$ would need to be scaled by the scintillation light
226 yield of the detector and an additional correction factor accounting for spatial
227 variations in the detector response. The additional scaling factors that describe
228 the light output of the detector are omitted here, as the signals were normalised
229 in data processing.

230     The PMMA degrader slabs were simulated using the NIST PMMA material
231 composition, setting the density such that the WET of the simulated slabs matched
232 the WET of the experimental slabs. For the anthropomorphic phantoms, voxelised
233 digital geometries were created from the treatment planning X-ray-CT scans. The
234 phantom materials were implemented from their chemical composition using the
235 material description in Niebuhr et al. (2019) and Niebuhr et al. (2016). See table 3
236 for a detailed list. First, for each Hounsfield unit (HU) in the CT scan, a material
237 was assigned based on the thresholds listed in table 3. Then the relative electron
238 density corresponding to the HU was calculated from the HU lookup table of the

    †The prototype features 2 mm, 2.6 mm as well as 3 mm sheets. In the simulation, a constant
binning of 3 mm was used.

*Mixed helium/carbon beam*                                                                11

239  CT scanner used to produce the treatment planning CTs. The relative electron
240  density was converted to physical density following equation 1 in Collins-Fekete
241  et al. (2017). This was then used to assign a material and density to each voxel of
242  the CT scan. For all voxels with a HU below -160 the assigned material was air
243  at density $1.155 \, \mathrm{mg/cm^3}$.

**Table 3.**  Chemical composition of the different materials used the anthropomorphic phantoms as implemented in the simulation. The HUs mark the lower-bound thresholds used for assigning a given material to voxel in the CT scans. The corresponding modelled patient tissue is given for each material.

| Material | HU | Element(weight(%)) | Tissue |
|---|---|---|---|
| Peanut oil | -160 | H(7.36);C(58.94);N(20.62);O(13.08) | Adipose |
| Agarose1 | -30 | H(10.57);C(0.94);O(84.49);Na(2.19);F(1.81) | Muscle |
| Agarose3 | 35 | H(10.82);C(1.65);O(86.53);Na(0.55);F(0.45) | Prostate |
| Vaseline/ $K_2HPO_4$ | 80 | H(5.52);C(64.6);N(5.02);O(9.19);P(4.45);K(11.22) | Inner bone |
| Gypsum | 285 | O(47.01);Ca(29.44);S(23.55) | Cortical bone |

244      For the anthropomorphic phantoms, additionally the dose deposit in each
245  voxel was recorded in the simulation. The dose in lateral direction was then
246  summed up to display the integral dose to the patient as function of the distance
247  to the isocentre.

248      All simulation results shown in this work were generated using $10^6$ primary
249  carbon ions and $10^5$ primary helium ions.

*2.5. Data processing and offline beam mixing*

251  In the experiment, helium and carbon beams were irradiated consecutively. The
252  experimental results shown in this work always represent a "snapshot" of the beam:
253  i.e. the sum of twenty-one image frames corresponding to a total acquisition time
254  of 0.84 seconds. Depth-light curves were generated from the background-corrected
255  images by summing up the light yield in a scintillator sheet and attributing it
256  to the WET at the centre of the sheet. The light yield is calibrated with two
257  shoot-through curves of the same ion taken from both sides of the range telescope
258  in order to correct for the differences in the signal of the scintillator sheets. The
259  depth-light curves of the helium and carbon beams were scaled according to a 10:1
260  carbon:helium ratio and summed up in order to produce the signal of a mixed
261  beam. In the simulation, the recorded signals were simply summed as a factor 10

*Mixed helium/carbon beam*                                                                    12

262 smaller number helium primaries compared to carbon had already been generated.
263 Figure 3 shows the resulting depth-light curves of helium, carbon and the mixed
264 helium/carbon beam. The curves were normalized to the combined helium/carbon
265 signal in the first scintillator sheet. Small differences are due to the fluctuations
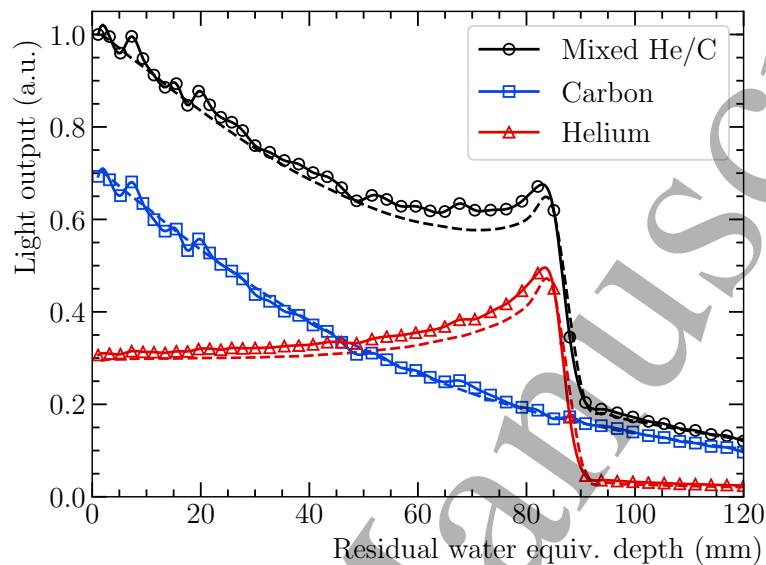266 in the measured carbon signal in the first couple of scintillator sheets.



**Figure 3.** Example of helium (red) and carbon (blue) depth-light curves used
for off-line helium-carbon beam mixing (black) at 220 MeV/u and the PMMA
setup without gap: measurement (solid) and simulation (dashed). The measured
signal for helium was scaled down to match a 10:1 ratio to the carbon primaries.

267 **3. Results**

268 In this section, the results from the irradiation of the phantoms introduced in
269 section 2.2 are presented. Both measurement and simulation results are presented
270 side by side for comparison. The relative difference between the curve of interest
271 $f(x)$ and a reference curve $g_{ref}(x)$ was chosen as a metric to quantify the change
272 in the measured signal. It is defined as $[f(x) - g_{ref}(x)]/g_{ref}(x)$. This enables
273 displaying very small differences between the curve of interest and the reference
274 curve, emphasising the sensitivity of the helium/carbon beam mixing. In all plots,
275 the horizontal axis represents the residual water equivalent range of the beam
276 measured in the scintillator stack. The depth-light curves were normalised to the

*Mixed helium/carbon beam*                                                    13

277 signal in the first scintillator sheet of the reference measurement in order to enable
278 easier comparison between experiment and simulation.

### 3.1. PMMA phantom

280 In figure 4, the effect of air slits of variable width and thickness are shown. The
281 5 mm and 2 mm slit widths resulted in respective relative differences of 40% and
282 20%. This is expected since, with increasing slit width, a larger fraction of beam
283 particles crosses the slit. For the 8 mm FWHM beam, approximately 55% of the
284 beam particles cross the slit opened to 5 mm width, while only ~22% of particles
285 traverse the slit in the case of an opening width of 2 mm. It can be seen in figure 4
286 (bottom) that the observed peak width in the relative difference is proportional
287 to the slit thickness. However, this relation is perturbed by the finite slope of the
288 helium peak and the limited spatial resolution of the range telescope. In all cases,
289 the mixed depth-light curve changed only slightly with the introduction of the air
290 gaps and those changes were only observable in the high-gradient region at the
291 helium peak.

### 3.2. ADAM phantom

293 The ADAM phantom was irradiated at three different spots in the same iso-
294 energy layer: the tumour isocentre, a spot close to the rectum according to the
295 treatment planning system (vertical position: isocentre-18 mm; horizontal position:
296 isocentre+6 mm) and a spot in between the two (vertical position: isocentre-
297 12 mm; horizontal position: isocentre). The spot positions and the different rectal
298 fillings are shown in figure 5.

299     Figure 6 shows the artificially mixed helium/carbon signals. For the spot close
300 to the rectum, a change in the helium range was observable even for the smallest
301 air volume filled in the rectal balloon. Since the rectum did not collapse when
302 the rectal balloon was not inflated, the lowest filling of the rectal balloon resulted
303 only in a small change of the diameter of the rectum compared to the reference
304 state. For larger fillings of the rectum, a drastic overshoot was observed in the
305 helium range as the beam crossed into the rectum and the rectal gas. Similarly,
306 for the spot located between isocentre and the rectal wall, the two larger rectal
307 balloon fillings resulted in observable changes in the helium signal. For the spot
308 in the isocentre, no significant change was observed for either air filling in the
309 measurement. In the simulation, however, small changes were observed for the
310 two larger air fillings. This disagreement could likely be attributed to changes
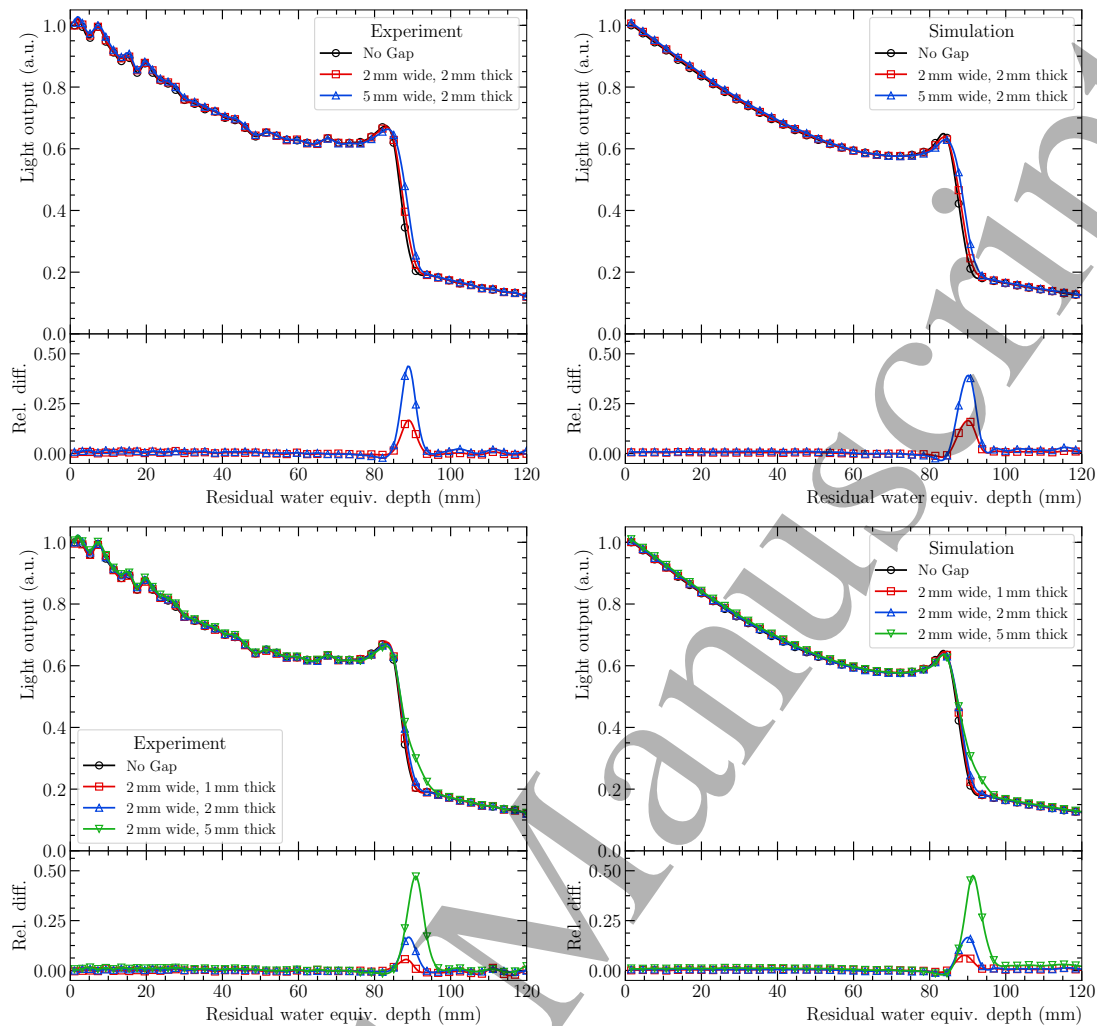
*Mixed helium/carbon beam* 14



**Figure 4.** Result of introducing an air-filled slit of width 2 to 5 mm and thicknesses of 2 mm and 5 mm (top), as well as a fixed width of 2 mm and thickness of 1 mm to 5 mm (bottom) in the beam path: measurement (left) and simulation (right).

in the relative distance of the spot centre to the urethra stemming from position uncertainties and/or motion of the prostate between the treatment planning CT and the irradiation. In the phantom the urethra is modelled with a silicone pipe. As such, the rectal balloon filling pushing the pipe wall out of the beam might have caused the observed range change in the simulation (compare figure 5). The measurements of the other two spots qualitatively agree well with the simulation. Additionally, the simulation shows that the position of the helium peak in the
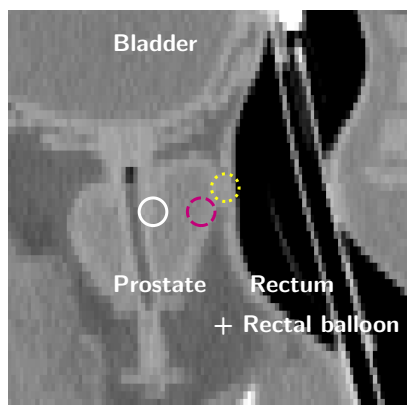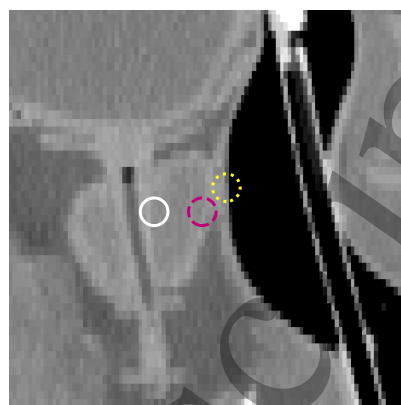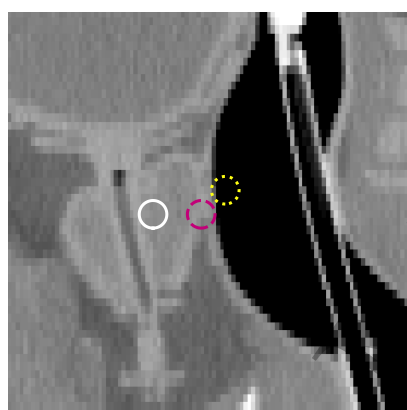
(a) No inflation

(b) 30 ml inflation

(c) 45 ml inflation

(d) 60 ml inflation

**Figure 5.** Sagittal plane of the ADAM phantom CT scans for different stages of inflation of the rectal balloon. The circles indicate the $2\sigma$ region of the irradiated carbon ion beam spots at the isocentre (white solid), close to the rectum (yellow dotted) and in between (magenta dashed).

318    detector correlates well with the changes in carbon dose in the patient (compare
319    figure 6b and c). This correlation is essential for drawing conclusions on the carbon
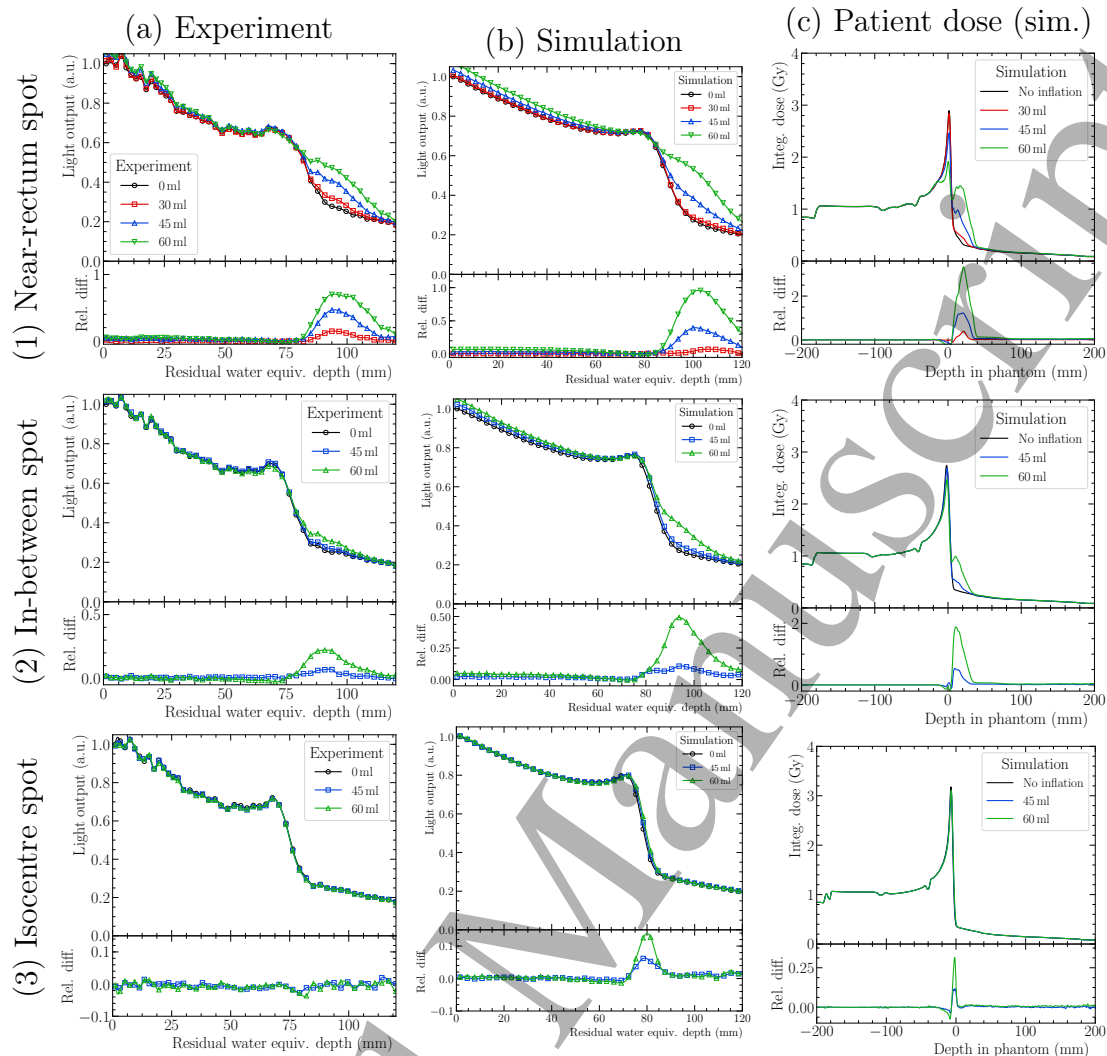320    dose from the mixed helium/carbon beam signal in the detector.

*Mixed helium/carbon beam*                                                      16



**Figure 6.** Detector response to different inflation stages of a rectal balloon placed in the rectum near the prostate for different beam spot positions: measured (left column) and simulated (middle column) helium/carbon beam signal in the detector. For comparison, the integrated dose to the phantom as a function of distance to the isocentre (right column) is shown. The dose considers both the helium and carbon beams.

### 3.3. ADAM-PETer phantom

In order to demonstrate the effect that a small patient rotation would have on the observed helium/carbon mixed signal, the ADAM-PETer phantom was used in its upright position, with the phantom rotated manually by $2°$ and $4°$ around the vertical axis. The results can be seen in figure 7. Both rotations lead to

*Mixed helium/carbon beam* 17

326 a noticeable change in the measured mixed beam signal. A similar, yet slightly
327 larger effect can be observed in the simulation. In the depth-dose profile shown in
328 figure 7(c), in addition to the range shift in the carbon peak, differences starting at
329 the position corresponding to the entrance of the hip bone (at ~135 mm upstream
330 from the isocentre) can be seen. As such, it can be argued that the observed shift
331 in the carbon range stems from the rotation of the hip bone.
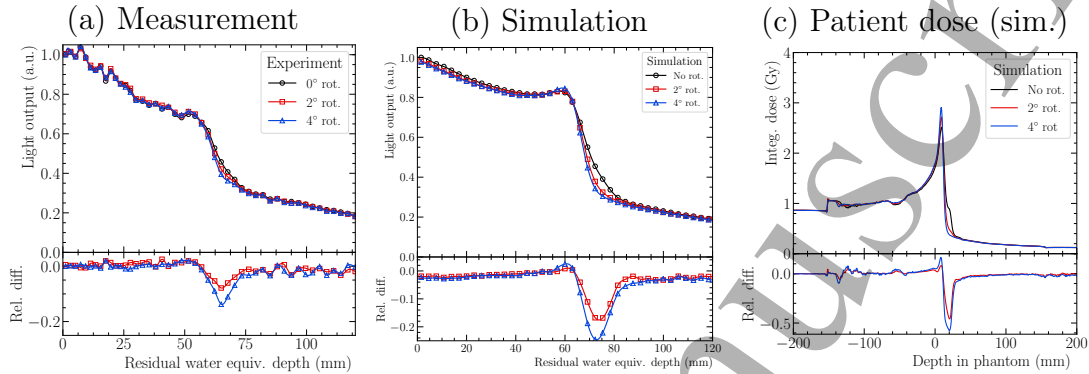


**Figure 7.** Result for different beam angles entering the phantom: measured
(a) and simulated (b) helium/carbon signal in the detector. (c) shows the
integrated dose to the patient as function of the distance to the isocentre. The
dose considers both the helium and the carbon ion.

## 332 4. Discussion

### 333 *4.1. Uncertainty sources*

334 *Detector readout and data processing:* Due to the high resolution of the CMOS
335 sensor and the high light output of the scintillator, the statistical uncertainty on
336 the light yield in a single sheet is low, $<1\%$ for carbon and helium.

337 However, the particle-specific calibration of the detector introduced a
338 systematic uncertainty, which was the same for all recorded curves of the same
339 particle. This uncertainty is estimated to be $<3\%$ by comparing the shoot-through
340 curves for protons, helium and carbon ions.

341 Furthermore, the carbon depth-light curves were acquired at a very low
342 beam intensity compared to the calibration shoot-through curves. This intensity
343 mismatch is likely to be responsible for the fluctuations seen in the carbon signal
344 (and therefore also in the mixed signal, see figure 3) close to the entrance of the
345 scintillator stack. These fluctuations are consistently the same for all measured

*Mixed helium/carbon beam* 18

346 depth-light curves (see figures 4, 6 and 7). The magnitude of the systematic
347 uncertainty in the low-intensity carbon signal is on the order of 5%.

348 *Particle rate:*   The mixing of the sequentially irradiated helium and carbon beam
349 in data processing required a stable particle rate to match a 10:1 ratio between
350 the carbon and helium signal. While this was the case for the standard beam
351 settings used, for the experimental beam parameters, fluctuations up to 15% were
352 observed between spills. For the experimental helium settings, no spill regulation
353 was active, likely causing these fluctuations. Hence, before adding the helium
354 and carbon signals together, for the pelvis phantom measurements, the helium
355 signals were scaled such that the signal in the first couple of sheets matched the
356 reference measurement for each phantom. As this normalisation step can only
357 cause an underestimation of signal changes, it does not affect the conclusion on
358 the usefulness of the helium/carbon beam mixing method.

359 *Beam parameters:*   There were slight differences in the beam parameters in the
360 standard libraries used for the irradiation of the PMMA setup. The small
361 mismatch between the beam energies of helium and carbon in the measurements
362 with the PMMA phantoms leads to a sub-millimetre shift of the helium and carbon
363 curves relative to each other compared to an actual mixed beam. This small shift
364 has no qualitative effect on the reported results since the slope of the carbon curve
365 beyond the Bragg peak is small and doesn't exhibit any prominent features. In the
366 case of the pelvis phantoms, a smaller helium spot was used compared to the carbon
367 spot, resulting in less range mixing (caused by lateral tissue inhomogeneities) as
368 would have been observed for a real mixed beam.

369 *Positioning uncertainty:*   Since the HIT experiment cave does not feature an
370 in-room imaging system, a source of uncertainty was the correct positioning of
371 the phantoms relative to the beam, compared with the treatment planning and
372 the simulation. For the PMMA setup, the slit was centered on the beam axis
373 marked by the in-room laser positioning system by opening the two PMMA slabs
374 symmetrically. In general a good agreement of simulation and measurement was
375 observed here, suggesting an accurate phantom positioning for the measurement.
376 For the ADAM phantom, the location of the target isocentre was marked on the
377 phantom surface based on the treatment plan CT scan. This process already
378 introduced some positioning uncertainty due to inaccuracies in the marking by
379 hand. For the ADAM-PETer phantom, the target isocentre was already marked

380 on the outside of the phantom with CT bead markers from an earlier experiment
381 which can be seen as bright spots on the phantom contour in figure 2(b). The in-
382 room positioning was then performed using the available laser positioning system.
383 Nevertheless, for both pelvis phantoms, all investigated beam spots were more than
384 2 mm away from the treatment field edge. Therefore, it can be argued that despite
385 positioning uncertainties, the results obtained still depict a realistic scenario.

386 　　In the ADAM-PETer measurements, an additional source of uncertainty was
387 the manual rotation of the phantom, since no automatic rotation was available.
388 Here, the angle relative to the isocentre position was manually drawn on the
389 phantom and is therefore subject to the same uncertainties mentioned above.
390 Nevertheless, the measurements serve to qualitatively demonstrate the feasibility of
391 observing small patient rotations/movements with a mixed helium/carbon beam.
392 It is important to mention that the CT bead markers were left on the ADAM-
393 PETer phantom during irradiation as well as in the simulation. While being made
394 from metal, they where spherical with a diameter of only 1.27 mm and are not
395 expected to have affected the measurement.

396 *Monte-Carlo simulation:*　The major uncertainty in the Monte-Carlo simulation
397 was the modeling of the phantom materials. Especially, for the anthropomorphic
398 phantoms, this introduced differences between the measured and the simulated
399 helium range. Due to noise and beam hardening artefacts in the CT image as well
400 as tissue substitute materials with overlapping Hounsfield unit range (Niebuhr
401 et al. 2019), it was not possible to match the simulated and real composition
402 perfectly with the method used in this work. For example, for the ADAM
403 phantoms, the silicone organ shells were simulated as inner bone, due to the overlap
404 in Hounsfield unit ranges for the two materials. Still, the observed signal variations
405 introduced by the investigated changes in the treated geometry qualitatively agree
406 well between simulation and experiment. However, when using Monte-Carlo
407 as a basis for comparison to generate online treatment feedback (see discussion
408 below), using more sophisticated methods to generate the Monte-Carlo material
409 composition — e.g. using a Dual-Energy CT image as the basis (Hünemohr
410 et al. 2014, Lalonde & Bouchard 2016) — would be adequate. Implementing
411 such methods, however, was beyond the scope of this work.

*Mixed helium/carbon beam* 20

### 4.2. Using a mixed helium/carbon beam for treatment monitoring

This work highlights the potential of mixing a small amount of helium ions with a therapeutic carbon-ion beam for observing changes in the treated anatomy. This corroborates previous studies using treatment planning software (Graeff et al. 2018) and experimental investigations with protons in place of helium ions (Mazzucconi et al. 2018). Since the helium energies are fixed by the carbon energies from the treatment plan, the helium/carbon beam mixing technique is limited to treatment directions were the proximal target edge is located deeper than 1/3 of the patient WET in that direction. Otherwise, the helium ions would not have sufficient energy to fully cross the patient leading to the helium Bragg peak being located in healthy tissue. However, this limitation can potentially be overcome by selecting the treatment direction accordingly, if the gained additional information from the helium ions out-weights the drawback of a non-ideal beam direction. A thorough evaluation of patient data is needed to assess the applicability of the helium/carbon mixing method for different treatment sites.

A general drawback of the method is that the helium ions are not only sensitive to range changes that affect the carbon ions, but also to every change that occurs distal to the tumour. However, integrating the tissue properties over the whole thickness of the patient rather than just up to the tumour volume is true for any radiography-based system. For patient sites where there is known anatomical motion distal to the tumour, such as lung cases, a pre-treatment 4D-CT should be used to relate a given motion phase to the helium range including also the distal anatomy. For prostate cases, on the other hand, this is a less critical limitation. Here, the expected motion scenarios involve, for example, hip motion/rotation, bladder and rectum filling, as well as muscle contractions around the prostate (Langen et al. 2008), which should have an effect on both the helium and carbon range. Additionally, since the prostate lies centrally in the patient for lateral beam directions, all treatment plan energies should be sufficiently high for the helium ions to fully cross the patient. Moreover, prostate cases might benefit greatly from the helium/carbon mixing method: the irregularity and randomness of the motion patterns makes prostate motion hard to predict or mitigate in scanned ion-beam therapy (Ammazzalorso et al. 2014), which is why online treatment feedback would be highly advantageous. This is even more important when considering hypo-fractionated carbon-beam therapy.

The biggest advantage of the helium/carbon mixing method is the high sensitivity. With the system used in this work, range changes as small as 1 mm

*Mixed helium/carbon beam*                                                              21

⁴⁴⁸ of less than a quarter particles in a pencil beam were observable. Furthermore,
⁴⁴⁹ this sensitivity is achieved for a small number of incident particles per spot since
⁴⁵⁰ only very few helium ions are required for a range measurement. It is important
⁴⁵¹ to note that for the measurements shown in this work a relatively large number of
⁴⁵² particles was integrated (21 readout frames summing up to $\sim 6.7 \times 10^7$ integrated
⁴⁵³ particles for the PMMA phantom measurements) compared to the number of
⁴⁵⁴ particles encountered in clinical pencil beams. This is due to the detector prototype
⁴⁵⁵ used not being the ideal detection system for the helium/carbon beam mixing
⁴⁵⁶ method, since it was developed as a quality assurance device for proton beams.
⁴⁵⁷ The amount of necessary particles could, however, be reduced by using a more
⁴⁵⁸ sensitive photodetector. A fast-enough detector might even enable the acquisition
⁴⁵⁹ of multiple range samples (snap shots) per beam spot (provided that the spot
⁴⁶⁰ contains enough particles) in order to observe motion trends.

⁴⁶¹     This work indicates that the previously suggested 10:1 ratio between primary
⁴⁶² carbon ions and helium ions is indeed useful for detecting changes in the treated
⁴⁶³ anatomy. However, the optimal mixing ratio will depend on the detector used as
⁴⁶⁴ well as on the technical aspects of the acceleration of the beam in the synchrotron.
⁴⁶⁵ Furthermore, the sensitivity of the method also depends on the beam spot size,
⁴⁶⁶ since with a smaller beam spot size small inhomogeneities would affect a larger
⁴⁶⁷ portion of the pencil beam particles. However, for the range telescope used in this
⁴⁶⁸ work, the lateral position of the artefact causing the observed range differences
⁴⁶⁹ could not be determined with better precision than the pencil beam size without
⁴⁷⁰ further processing. In order to achieve a better spatial resolution, the information
⁴⁷¹ of adjacent spots in the treatment plan could be matched (Hammi et al. 2017) or
⁴⁷² position sensitive detectors could be included to the setup (see for example Krah
⁴⁷³ et al. (2018) for an overview over the spatial resolution of different particle imaging
⁴⁷⁴ setups).

⁴⁷⁵     It is not trivial to quantify the observed changes in the helium range due to
⁴⁷⁶ the strong range mixing in heterogeneous materials. A possible option would be
⁴⁷⁷ to conduct a multi Bragg-peak fit similar to the methodology developed in Krah
⁴⁷⁸ et al. (2015). In the work described here, the relative difference to a reference
⁴⁷⁹ measurement was used to quantify range changes. This enables quantifying
⁴⁸⁰ small changes compared to the expected signal without relying on a single point
⁴⁸¹ of reference and without the need to perform a fit to the signal. The latter
⁴⁸² feature could be of importance when using a mixed helium/carbon beam for
⁴⁸³ generating online feedback during the treatment where computational speed is
⁴⁸⁴ a necessity. On the other hand, using the relative difference compared to the

*Mixed helium/carbon beam* 22

485 expected signal as a metric requires generating a reference curve for every beam
486 spot. This could potentially be accomplished using Monte Carlo simulations at
487 the treatment planning stage that include an accurate description of the detector
488 output (including spatial variations in the detector response/scintillation light
489 quenching) and patient geometry, as has been suggested in Mazzucconi et al.
490 (2018). As stated above, this would require sophisticated tissue decomposition
491 methods, as well as accurate physics models in the simulation. Nevertheless, an
492 accurate representation of the patient is crucial for treatment planning and, hence,
493 an observed deviation from the expected signal would point towards a potential
494 uncertainty in the treatment plan.

495 Finally, a mixed helium/carbon beam would offer the potential for post-
496 treatment reconstruction of 2D images of the treated anatomy for each iso-energy
497 slice using the techniques developed for particle radiographic imaging (cf. Parodi
498 (2014), Krah et al. (2015)). This could be useful in post-treatment patient-specific
499 quality assurance and dose accumulation.

500 However, whilst the presented results are indicative of the potential of a mixed
501 beam, they can only serve as a conceptual assessment of the method since they were
502 produced with sequentially irradiated helium/carbon beams. Definitive statements
503 of the usefulness of such a technique can only be made based on a real mixed beam.

### 504 *4.3. Acceleration of a mixed helium/carbon beam*

505 As also reported in Mazzucconi et al. (2018), the most straightforward way to
506 generate a mixed beam would be to mix the two ions at the sources. However,
507 at HIT, a reasonable current of $^{12}C^{6+}$ cannot be extracted from the sources.
508 Hence, one would extract $^{12}C^{3+}$ and $^4He^+$ from a source running with methane‡
509 as the main gas and helium as the support gas. With a similar mass/charge
510 ratio ($A/q \approx 4$), the partially stripped ions could pass the injection beam line
511 together. However, the HIT LINAC pre-accelerator is optimised to accelerate
512 ions with $A/q \leq 3$ and cannot accelerate ions with $A/q=4$. Therefore, a real mixed
513 helium/carbon beam could not yet be delivered. A potential workaround to this
514 issue could be to fully strip the ions before the LINAC instead of the current
515 stripping after the LINAC, although this is usually avoided since the stripping
516 efficiency decreases with decreasing beam energy (Bryant et al. 2000). Another
517 possibility would be to achieve the beam mixing in the synchrotron by sequentially

‡For the usually used $CO_2$ gas, the $^{12}C^{3+}$ peak in the source spectrum would overlap with
the $^{16}O^{4+}$ peak.

*Mixed helium/carbon beam* 23

518 injecting the different ions. Since $^{16}O^{4+}$ could also pass the low energy beam
519 transport together with $^{12}C^{3+}$ and $^4He^+$, mixing the beam inside the synchrotron
520 might be preferable in order to avoid beam contamination with oxygen ions.
521 The acceleration of a mixed beam will be the subject of further investigation.
522 Nevertheless, since a great effort is usually made to avoid the contamination of
523 the accelerated ion beams with ions of similar mass/charge ratio (cf. Winkelmann
524 et al. (2008)), there is a strong reasoning that such a contamination could also be
525 generated deliberately. If a mixed beam in the synchrotron can be generated, stable
526 extraction, beam focusing and pencil beam scanning will add further complexity.
527 Still, from the results presented in this work it is possible to conclude that the
528 concept of a mixed beam for simultaneous treatment and imaging deserves further
529 investigation.

530 *4.4. Advantages of beam mixing versus sequential irradiation*

531 Given the complexity of the acceleration of a mixed beam, the question arises if
532 intra-fractional treatment monitoring could also be achievable with sequentially
533 irradiated beams. Sequential beams come at the advantage of being easier to
534 generate compared to a mixed beam. Moreover, the verification beam would not
535 be limited by the parameters of the treatment plan. For patient sites subject
536 to slow motion, sequential verification and treatment beams could provide useful
537 information, if fast switching of ion sources or beam energy is technically feasible
538 which is currently being investigated at HIT (Schömers et al. 2017). In that case,
539 changes would be detected with a probably tolerable delay, depending on the rate
540 of verification to treatment spills and the time needed for switching sources/beam
541 energy. Still, an online range estimate provided by a mixed beam would improve
542 the potential for reduction of unwanted dose delivery and the accuracy of post hoc
543 dose reconstruction for adaptive therapy.

544 For the treatment of moving targets, especially those with strong range
545 changes such as lung tumors, a mixed beam would be most advantageous. Here,
546 online motion information is most relevant, even if it is only used for dose
547 reconstruction and possible adaptation of following fractions. An important
548 aspect is also that with a mixed beam every spot in a treatment plan could be
549 monitored without prolonging the treatment duration. This would be preferential
550 for the clinical environment at an ion-beam therapy facility where short treatment
551 duration is highly desired (Schömers et al. 2017). Nevertheless, in future studies,
552 the usefulness of sequential beams for verification should also be further evaluated

*Mixed helium/carbon beam* 24

553 especially for static or non-periodically moving targets such as the prostate.

## 5. Conclusion

555 In this work the use of a mixed helium/carbon beam for monitoring intra-fractional
556 anatomical changes was investigated using a novel range telescope. It was
557 demonstrated that with a mixed beam, range changes as small as 1 mm of only a
558 fraction of the beam width could be observed with the system despite the presence
559 of range mixing. Using two anthropomorphic phantoms, the method's use in more
560 realistic clinical cases was investigated. Here, it was demonstrated that a mixed
561 helium/carbon beam could be useful for observing bowel gas movements and small
562 patient rotations. A limitation of the technique is that the helium energies are
563 determined by the carbon treatment plan and thus might not have sufficient energy
564 to cross the patient for all treatment fields/patient sites. Furthermore, the helium
565 signal will integrate any uncertainty located distal to the carbon peak. Future
566 studies should hence involve 4D patient data to identify patient sites that would
567 benefit most from the technique. The generation of a real mixed helium/carbon
568 beam at a synchrotron accelerator is a subject for further investigations.

## Author contributions

570 LV was in charge of planning and preparing the experiments and carried out
571 the simulations presented in this work. LK operated the detector during the
572 experiment and conducted the processing of the experimental data. LV and LK
573 equally shared the writing of the manuscript and the analysis/discussion of the
574 acquired results. All authors contributed significantly to the presented work.

*Mixed helium/carbon beam* 25

## References

589 Agostinelli, S., Allison, J., Amako, K., Apostolakis, J., Araujo, H. et al. (2003). Geant4—a
590     simulation toolkit, *Nuclear Instruments and Methods in Physics Research Section A:*
591     *Accelerators, Spectrometers, Detectors and Associated Equipment* **506**(3): 250–303.
592 Allison, J., Amako, K., Apostolakis, J., Araujo, H., Dubois, P. A. et al. (2006). Geant4
593     developments and applications, *IEEE Transactions on Nuclear Science* **53**(1): 270–278.
594 Allison, J., Amako, K., Apostolakis, J., Arce, P., Asai, M. et al. (2016). Recent developments in
595     geant4, *Nuclear Instruments and Methods in Physics Research Section A: Accelerators,*
596     *Spectrometers, Detectors and Associated Equipment* **835**: 186 – 225.
597     **URL:** *http://www.sciencedirect.com/science/article/pii/S0168900216306957*
598 Ammazzalorso, F., Graef, S., Weber, U., Wittig, A., Engenhart-Cabillic, R. & Jelen, U.
599     (2014). Dosimetric consequences of intrafraction prostate motion in scanned ion beam
600     radiotherapy, *Radiotherapy and Oncology* **112**(1): 100 – 105.
601 Arico, G. (2016). *Ion Spectroscopy for improvement of the Physical Beam Model for Therapy*
602     *Planning in Ion Beam Therapy*, PhD thesis, The Faculty of Physics and Astronomy,
603     Heidelberg University.
604 Berger, M. J., Coursey, J. S., Zucker, M. A. & Chang, J. (2005). *ESTAR, PSTAR and ASTAR:*
605     *Computer Programs for Calculating Stopping-Power and Range Tables for Electrons,*
606     *Protons and Helium Ions*, National Institue of Standards and Technology.
607     **URL:** *http://physics.nist.gov/Star*
608 Bert, C., Grözinger, S. O. & Rietzel, E. (2008). Quantification of interplay effects of scanned
609     particle beams and moving targets, *Physics in Medicine and Biology* **53**(9): 2253–2265.
610 Birks, J. B. (1951). Scintillations from organic crystals: Specific fluorescence and relative
611     response to different radiations, *Proc. Phys. Soc.* **A64**: 874–877.
612 Bryant, P. J. et al. (2000). Proton-Ion Medical Machine Study (PIMMS), 2.
613 Böhlen, T. T., Cerutti, F., Dosanjh, M., Ferrari, A., Gudowska, I., Mairani, A. & Quesada, J. M.
614     (2010). Benchmarking nuclear models of FLUKA and GEANT4 for carbon ion therapy,
615     *Physics in Medicine and Biology* **55**(19): 5833–5847.
616 Collins-Fekete, C.-A., Brousmiche, S., Hansen, D. C., Beaulieu, L. & Seco, J. (2017). Pre-
617     treatment patient-specific stopping power by combining list-mode proton radiography
618     and x-ray ct, *Physics in Medicine and Biology* **62**(17): 6836.
619     **URL:** *http://stacks.iop.org/0031-9155/62/i=17/a=6836*
620 Dolde, K., Naumann, P., Dávid, C., Gnirs, R., Kachelrieß, M., Lomax, A. J., Saito, N., Weber,
621     D. C., Pfaffenberger, A. & Zhang, Y. (2018). 4d dose calculation for pencil beam scanning
622     proton therapy of pancreatic cancer using repeated 4dmri datasets, *Physics in Medicine*
623     *& Biology* **63**(16): 165005.
624 Dudouet, J., Cussol, D., Durand, D. & Labalme, M. (2014). Benchmarking geant4 nuclear
625     models for hadron therapy with 95 mev/nucleon carbon ions, *Phys. Rev. C* **89**: 054616.

*Mixed helium/carbon beam*          26

Ferrero, V., Fiorina, E., Morrocchi, M., Pennazio, F., Baroni, G. et al. (2018). Online proton therapy monitoring: clinical test of a silicon-photodetector-based in-beam pet, *Scientific Reports* **8**(1): 4100.
     **URL:** *https://doi.org/10.1038/s41598-018-22325-6*

Graeff, C., Weber, U., Schuy, C., Saito, N., Volz, L., Piersimoni, P., Seco, J. & Kraemer, M. (2018). [oa027] Helium as a range probe in carbon ion therapy, *Physica Medica: European Journal of Medical Physics* **52**: 11.
     **URL:** *https://doi.org/10.1016/j.ejmp.2018.06.099*

Haberer, T., Debus, J., Eickhoff, H., Jäkel, O., Schulz-Ertner, D. & Weber, U. (2004). The heidelberg ion therapy center, *Radiotherapy and Oncology* **73**: S186–S190.
     **URL:** *http://dx.doi.org/10.1016/S0167-8140(04)80046-X*

Hammi, A., Lomax, T. & Weber, D. (2017). Su-f-601-1: A new technique for increasing spatial resolution of proton radiography, Presented at the American Association of Physics in Medicine annual meeting, Denver, USA.
     **URL:** *https://www.aapm.org/meetings/2017AM/PRAbs.asp?mid=127&aid=37891*

Homolka, N., Pfaffenberger, A., Beuthien-Baumann, B., Mann, P., Schneider, V. et al. (2019). Pv-0479: Development of an anthropomorphic multimodality pelvis phantom for pet/mri- and ct-based radiation treatment planning of prostate cancer, *Radiotherapy & Oncology* **133**(1).

Horst, F., Aricò, G., Brinkmann, K.-T., Brons, S., Ferrari, A. et al. (2019). Measurement of $^4$He charge- and mass-changing cross sections on h, c, o, and si targets in the energy range 70–220 mev/u for radiation transport calculations in ion-beam therapy, *Phys. Rev. C* **99**: 014603.

Hueso-González, F., Rabe, M., Ruggieri, T. A., Bortfeld, T. & Verburg, J. M. (2018). A full-scale clinical prototype for proton range verification using prompt gamma-ray spectroscopy, *Physics in Medicine & Biology* **63**(18): 185019.
     **URL:** *https://doi.org/10.1088%2F1361-6560%2Faad513*

Hünemohr, N., Paganetti, H., Greilich, S., Jäkel, O. & Seco, J. (2014). Tissue decomposition from dual energy CT data for MC based dose calculation in particle therapy, *Medical Physics* **41**(6): 061714.

Kanai, T., Furusawa, Y., Fukutsu, K., Itsukaichi, H., Eguchi-Kasai, K. & Ohara, H. (1997). Irradiation of mixed beam and design of spread-out bragg peak for heavy-ion radiotherapy, *Radiation Research* **147**(1): 78–85.

Kleffner, C., Ondreka, D. & Weinrich, U. (2009). The heidelberg ion therapy (hit) accelerator coming into operation, *AIP Conference Proceedings* **1099**(1): 426–428.
     **URL:** *http://aip.scitation.org/doi/abs/10.1063/1.3120065*

Krah, N., Khellaf, F., Létang, J. M., Rit, S. & Rinaldi, I. (2018). A comprehensive theoretical comparison of proton imaging set-ups in terms of spatial resolution, *Physics in Medicine & Biology* **63**(13): 135013.

Krah, N., Testa, M., Brons, S., Jäkel, O., Parodi, K., Voss, B. & Rinaldi, I. (2015). An advanced image processing method to improve the spatial resolution of ion radiographies, *Physics in Medicine and Biology* **60**(21): 8525.
     **URL:** *http://stacks.iop.org/0031-9155/60/i=21/a=8525*

Lalonde, A. & Bouchard, H. (2016). A general method to derive tissue parameters for Monte Carlo dose calculation with multi-energy CT, *Physics in Medicine and Biology*

*Mixed helium/carbon beam*                                                                 27

671    **61**(22): 8044.

672    **URL:** *http://stacks.iop.org/0031-9155/61/i=22/a=8044*

673    Langen, K. M., Willoughby, T. R., Meeks, S. L., Santhanam, A., Cunningham, A., Levine,
674        L. & Kupelian, P. A. (2008). Observations on real-time prostate gland motion using
675        electromagnetic tracking, *International Journal of Radiation Oncology\*Biology\*Physics*
676        **71**(4): 1084 – 1090.

677    Mazzucconi, D., Agosteo, S., Ferrarini, M., Fontana, L., Lante, V., Pullia, M. & Savazzi, S.
678        (2018). Mixed particle beam for simultaneous treatment and online range verification in
679        carbon ion therapy: Proof-of-concept study, *Medical Physics* **45**(11): 5234–5243.

680    **URL:** *https://aapm.onlinelibrary.wiley.com/doi/abs/10.1002/mp.13219*

681    Niebuhr, N. I., Johnen, W., Echner, G., Runz, A., Bach, M., Stoll, M., Giske, K., Greilich, S. &
682        Pfaffenberger, A. (2019). The ADAM-pelvis phantom—an anthropomorphic, deformable
683        and multimodal phantom for MRgRT, *Physics in Medicine & Biology* **64**(4): 04NT05.

684    Niebuhr, N. I., Johnen, W., Güldaglar, T., Runz, A., Echner, G., Mann, P., Möhler, C.,
685        Pfaffenberger, A., Jäkel, O. & Greilich, S. (2016). Technical note: Radiological properties
686        of tissue surrogates used in a multimodality deformable pelvic phantom for mr-guided
687        radiotherapy, *Medical Physics* **43**(2): 908–916.

688    Paganetti, H. (2012). Range uncertainties in proton therapy and the role of Monte Carlo
689        simulations, *Physics in Medicine and Biology* **57**(11): R99.

690    **URL:** *http://iopscience.iop.org/0031-9155/57/11/R99*

691    Parodi, K. (2014). Heavy ion radiography and tomography, *Physica Medica* **30**(5): 539 – 543.
692        Particle Radiosurgery Conference.

693    **URL:** *http://www.sciencedirect.com/science/article/pii/S1120179714000271*

694    Parodi, K. & Polf, J. C. (2018). In vivo range verification in particle therapy, *Medical Physics*
695        **45**(11): e1036–e1050.

696    Schömers, C., Feldmeier, E., Galonska, M., Horn, J., Peters, A. & Haberer, T. (2017). Thpva083:
697        First tests of a re-accelerated beam at heidelberg ion-beam therapy center (hit), *in*
698        V. R. W. Schaa, G. Arduini, M. Lindroos & J. Pranke (eds), *Proceedings of IPAC2017*,
699        JACoW.

700    Seco, J., Robertson, D., Trofimov, A. & Paganetti, H. (2009). Breathing interplay effects
701        during proton beam scanning: simulation and statistical analysis, *Physics in Medicine*
702        *and Biology* **54**(14): N283–N294.

703    Tripathi, R., Cucinotta, F. & Wilson, J. (1999). Accurate universal parameterization of
704        absorption cross sections iii – light systems, *Nuclear Instruments and Methods in Physics*
705        *Research Section B: Beam Interactions with Materials and Atoms* **155**(4): 349 – 356.

706    Wieser, H.-P., Cisternas, E., Wahl, N., Ulrich, S., Stadler, A. et al. (2017). Development
707        of the open-source dose calculation and optimization toolkit matrad, *Medical Physics*
708        **44**(6): 2556–2568.

709    **URL:** *http://dx.doi.org/10.1002/mp.12251*

710    Winkelmann, T., Cee, R., Haberer, T., Naas, B., Peters, A., Scheloske, S., Spädtke, P. &
711        Tinschert, K. (2008). Electron cyclotron resonance ion source experience at the heidelberg
712        ion beam therapy center, *Review of Scientific Instruments* **79**(2): 02A331.